Finite Element Modelling of Trabecular Bone Microstructure using Emerging CT Images

Indranil Guha,[a*] Chamith S. Rajapakse,[b] Xiaoliu Zhang,[a] Gregory Chang,[c] Punam K Saha[a,d]

[a]Department of Electrical and Computer Engineering, College of Engineering, University of Iowa, IA 52242
[b]Department of Radiology and Orthopaedic Surgery, University of Pennsylvania, PA 19104
[c]Department of Radiology, New York University Grossman School of Medicine, NY 10016
[d]Department of Radiology, Carver College of Medicine, University of Iowa, Iowa City, IA 52242

ABSTRACT

Osteoporosis is a common age-related disease associated with increased bone loss causing reduced bone strength and enhanced fracture-risk. Finite element (FE) modelling is used to estimate bone strength from high-resolution three-dimensional (3-D) imaging modalities including micro-CT, MRI, and HR-pQCT. Emerging technologies of multi-row detector CT (MDCT) imaging offer spatial image resolution comparable to human trabecular thickness. However, at the current MDCT resolution regime, FE modelling based on segmented trabecular bone (Tb) microstructure suffers from noise and other imaging artifacts. In this paper, we present a bone mineral density (BMD)-adjusted FE modeling method of Tb microstructure from MDCT imaging without requiring Tb segmentation. The method spatially varies mechanical stiffness based on local ash-density estimated from MDCT-derived calcium hydroxyapatite (CHA) density and, thus, models the hypothesis that stress-flow is primarily absorbed by Tb microstructure as compared to marrow space under mechanical compression. Specifically, an MDCT-based linear FE analysis method was developed using a voxel-mesh and the above model of space-varying stiffness, and the performance of the method was examined. For FE analysis, an axial cylindrical image core of 8mm diameter from 4-6% of distal tibia was extracted after aligning the tibial bone axis with the coordinate z-axis of the image space. Intra-class correlation coefficient (ICC) of 0.98 was observed in a repeat MDCT scan reproducibility experiment using cadaveric distal tibia specimens (n = 10). Also, high linear correlation (r = 0.87) was found between von Mises stress values and MDCT based CHA at individual voxels supporting the central hypothesis of our method.

Keywords: Osteoporosis, MDCT imaging, trabecular bone microstructure, ash density, linear finite element analysis (FEA), von Mises stress, Young's modulus, ANSYS software.

1. INTRODUCTION

Osteoporosis is a bone disease prevalent among older population and associated with reduce bone mineral density (BMD) and increased fracture-risk.[1,2] A study by Wright *et al*. in 2010 estimated that 10.2 million adults over the age of 50 years had osteoporosis in the United States alone.[3] Nearly, one in four men and one in two women suffer one or more fragility fractures in their lifetime.[4] Although hip, forearm, spine, pelvis, distal femur, wrist, and humerus are the common sites for osteoporotic fractures, hip fractures are clinically most devastating ones.[5] Osteoporosis remains undetected until a fracture occurs as bone becomes highly fragile at the advanced stages of the disease and bone imaging plays an important role in the assessment of bone quality and improved diagnosis of osteoporosis.[6,7] Dual-energy x-ray absorptiometry (DXA) computed areal BMD is the clinical standard for characterization of osteoporosis. However, BMD explains 60%-70% of the bone's mechanical competence and the remaining is explained by the collective effect of several other factors such as trabecular bone (Tb) strength and their microstructural basis.[8-11]

Finite element (FE) modelling is widely used to computationally estimate bone strength and other mechanical properties.[12-16] Recent technological advances in several three-dimensional (3-D) imaging modalities, including micro-CT imaging, magnetic resonance imaging (MRI),[17-20] and high-resolution peripheral quantitative computed tomography (HR-pQCT),[21-

*indranil-guha@uiowa.edu

[23] have enabled *in vivo* acquisition of Tb microstructure and allowed researchers to model computational bone mechanics at microstructural details.

Among *in vivo* imaging modalities, HR-pQCT and MRI have drawn major attention in FE modelling of bone at distal and proximal sites due to their potential in monitoring alterations in bone mechanical properties resulting from disease progression or drug intervention.[24-29] Several studies have demonstrated that FE modelling of Tb from HR-pQCT images is capable of assessing bone strength and fracture-risk.[16,28,30-33] Specifically, QCT derived ash density has been shown to be highly associated with mechanical properties of trabecular and cortical bone before, during and after failure under compression in all anatomic directions.[30] However, there are few works available in literature on FE analysis (FEA) of Tb using multi-row detector CT (MDCT) imaging,[34,35] although it offers *in vivo* spatial image resolution comparable to human trabecular thickness and provides quantitative BMD at individual voxels and overcomes the major deficits of MRI and HR-pQCT modalities related to slow scan speed and limited field-of-view.[36] Primary reason being, at the current MDCT resolution regime mesh modeling and. FEA using segmentation of Tb microstructure suffers from noise and other imaging artifacts. In this paper, we present an MDCT-based FEA method that does not require segmentation of Tb microstructure. Instead, the method models computational mechanics of Tb microstructure using BMD-adjusted stiffness. Specifically, the FEA method uses ash-density, estimated from MDCT measured BMD derived calcium hydroxyapatite (CHA) density, to define stiffness of individual voxels. In other words, the model simulates an FEA method along the hypothesis that stress-flow is primarily absorbed by Tb microstructure as compared to marrow space under mechanical compression. We have defined the materials used in our experiments and the MDCT-based FEA method as well as the experimental and data analysis plans in Section 2. Experimental results are presented in Section 3 and finally conclusions are drawn in Section 4.

2. METHODOLOGY

In this section we describe our method and experimental plans to evaluate the MDCT-based FEA method. Toward this goal the following material and methods were used — (1) cadaveric ankle specimens, (2) MDCT imaging, (3) image pre-processing, (4) BMD-adjusted linear FE modelling and analysis, and (5) experiments and data analysis.

2.1 Cadaveric Ankle Specimens

Ten fresh-frozen cadaveric ankle specimens were collected under the Deeded Bodies Program at the University of Iowa, Iowa City, IA. Specimens from donors with history of bone tumor, metastasis, or fracture at tibia were excluded from MDCT imaging. The specimens were separated at mid-tibia and soft tissues as well as the ankle joint and foot were preserved. The specimens were kept frozen in sealed plastic bags and were thawed at room temperature before MDCT imaging.

2.2 MDCT Imaging

MDCT imaging was performed on a 128 slice SOMATOM Definition Flash scanner (Siemens, Munich, Germany) at the University of Iowa Comprehensive Lung Imaging Center. Single tube spiral acquisition with the following CT parameters were used to generate high-resolution Tb images — 120 kV, 200 effective mAs, 1 sec rotation speed, pitch factor: 1.0, number of detector rows: 16, scan time: 23.2 secs, collimation: 16 × 0.6 mm, total effective dose equivalent: 170μSv ≈ 20 days of environmental radiation in the U.S. Siemens z-UHR scan mode was applied, which enables Siemens double z sampling technology allowing a dual sampling of the 0.6 mm detectors, splitting the signal so that each detector created a 0.3 mm slice in the z plane. After scanning in a helical mode with a 400 μm slice thickness, images were reconstructed at 200 μm slice-spacing using a normal cone beam method with a special U70u kernel achieving high structural resolution.

2.3 Image Pre-Processing

Ankle MDCT scans were rotated to align the tibial bone axis with the coordinate z-axis to make the longitudinal trabeculae predominantly upright. After bone alignment upright cylindrical volume of interests (VOI) were harvested for FEA. Also, BMD (g/cc) values derived from CT Hounsfield unit (HU) numbers were mapped into CHA density (g/cc).

2.3.1 Bone Alignment and VOI Selection

The tibial bone region was segmented from MDCT scans using soft thresholding, connectivity analysis and morphological operations and the tibial bone axis was computed over the 40% peeled region proximal to 8% distal site.[37] After computation of bone axis MDCT scans were rotated to align the bone axis with coordinate z-axis and interpolated to 150 μm isotropic voxels using the windowed-sync method.[38] Bone alignment and isotropic voxel interpolation steps were

performed simultaneously to reduce the image resolution loss due to interpolation. Finally, cylindrical VOIs of 8 mm diameter covering 4-6% of distal tibial site (~6.75 mm in length) were selected for FEA with their axis aligned to the respective bone axis. The cross-sectional diameter of the VOIs were always greater than the axial length to reduce microstructural disintegrity effects near the surface.[39]

2.3.2 Conversion of HU numbers into CHA Density

MDCT intensity was mapped into CHA density in two-steps – first MDCT intensities were converted into BMD using a Gammex RMI 467 Tissue Characterization Phantom (Gammex RMI, Middleton, WI).[40] The CHA density value at a voxel p, denoted by $\rho_{\mathrm{CHA}}(p)$, was obtained from the BMD value $\rho_{\mathrm{BMD}}(p)$ using known density values D_{CHA} (3.18 g/cc) and D_{water} (1 g/cc) and the following linear equation

$$\rho_{\mathrm{CHA}}(p) = \frac{(\rho_{\mathrm{BMD}}(p) - D_{\mathrm{water}})}{(D_{\mathrm{CHA}} - D_{\mathrm{water}})} \times D_{\mathrm{CHA}}. \quad (1)$$

2.4 BMD-Adjusted Linear FE Modelling and Analysis

A compressive FEA method was developed for an upright cylindrical Tb region at an isotropic image resolution. The method directly uses the interpolated voxel grid to define the mesh structuring elements. Each voxel is modelled as a cubical element with its center aligned at the voxel coordinate location, and edges are added following the network of the cubical complex representation of a voxel grid.[41] The connectivity within the FE mesh is defined by specifying common vertex and edge elements between each pair of adjacent voxel or cubical elements. Isotropic mechanical material properties are assigned to each cubic element, where elastic modulus of a cubical element is derived from the CHA density value at the corresponding voxel. Let p_{e} denote the cubical mesh element corresponding to the image voxel p; also, let $\rho_{\mathrm{CHA}}(p)$ denote the CHA density at p computed from MDCT derived BMD value $\rho_{\mathrm{BMD}}(p)$ at that voxel. The ash density (g/cc) value at p, denoted by $\rho_{\mathrm{ash}}(p)$, is computed from $\rho_{\mathrm{CHA}}(p)$ using the following equation[16]

$$\rho_{\mathrm{ash}}(p) = 0.0633 + 0.887\rho_{\mathrm{CHA}}(p). \quad (2)$$

The elastic modulus (MPa) of the cubical mesh element p_{e} corresponding to the image voxel p, denoted by $E(p_{\mathrm{e}})$, is derived from $\rho_{\mathrm{ash}}(p)$ following the equation by Keyak *et al.*[30]

$$E(p_{\mathrm{e}}) = 21700 \cdot \rho_{\mathrm{ash}}^{2.07}(p). \quad (3)$$

Finally, a Poisson's ratio of 0.3 is assigned to all elements.[15] Boundary conditions are imposed to simulate a physical mechanical experiment of axial compressive loading. Specifically, the bottom surface of the cylindrical VOI is fixed in all three coordinate directions, and a constant displacement along the coordinate z-direction is applied on all vertices at the top surface while restricting their movements along the x- and y-directions.

The method was designed and implemented within the computational platform and facilities provided by the ANSYS software (ANSYS Mechanical 2019 R2, Ansys Inc., Southpointe, Pennsylvania, USA) on a Linux machine equipped with 64 GB RAM, 72 cores Intel(R) Xeon(R) Gold 6240 CPU @ 2.60 GHz processor, and four Tesla V100-SXM2 GPUs with 32 GB memory each. The 3-D 8-Node structural solid (SOLID185) within the ANSYS software was selected to represent cubic mesh elements, and a linear equation solver was applied with an automatic time-stepping option. The boundary conditions were imposed as described earlier and a total displacement of 0.067 mm (~1% of the VOI length) was applied on the BMD-adjusted FE mesh model over 10 iterations. Finally, Young's modulus (or modulus) was computed as the ratio of average von Mises stress (MPa)[42] of volume elements on the VOI top surface and applied displacement.

2.5 Experiments and Data Analysis

Experiments were designed to evaluate — (1) the relationship between CHA density and stress, and (2) repeat scan reproducibility of the FEA method. To determine the relationship between CHA density and stress, linear correlation coefficient (r-value) between CHA density value and observed von Mises stresses at individual voxels on the middle axial slice of all ten specimens was computed; the image and FEA data of the first scan of each specimen was used for this analysis. Intra-class correlation coefficient (ICC) of computed modulus values from repeat CT scans was calculated to examine the reproducibility of the method. Bone filling, upright bone alignment, VOI selection, and FEA steps were independently applied on repeat CT scans to determine reproducibility of the combined process including CT imaging as well as the comprehensive analytic protocol.

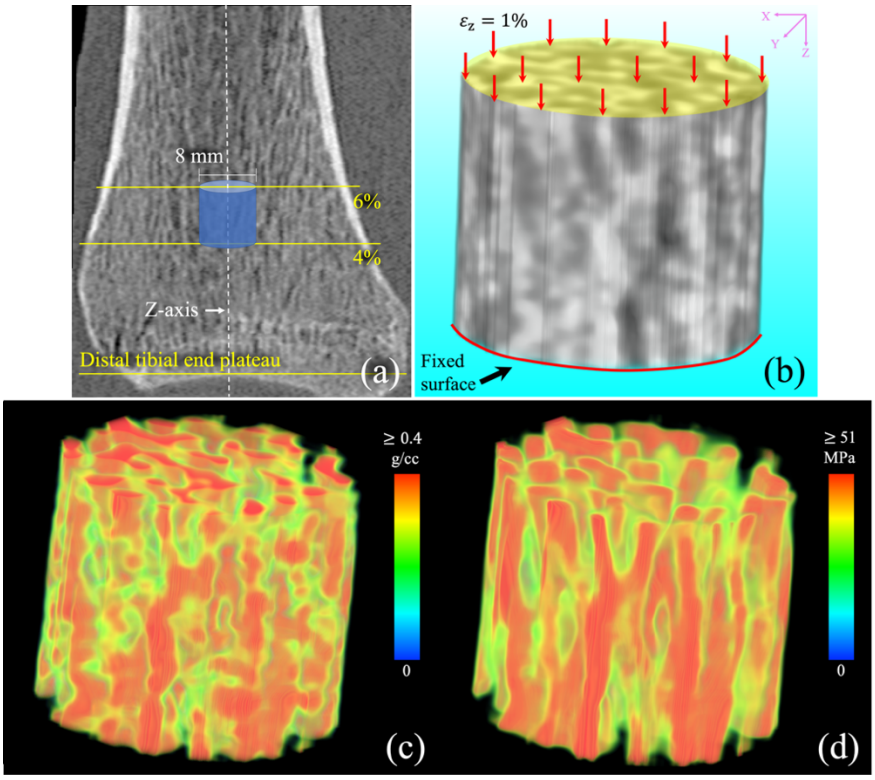

Figure 1. Multi-row detector CT-based FE modelling and computation of trabecular microstructural strength. (a) A sagittal image slice from a distal tibia MDCT scan; the cylindrical VOI for FEA is shown in blue. (b) FEA boundary condition and loading protocol on the extracted Tb core. (c) Color-coded volume rendition of the CHA density map over the VOI of (b). (d) Same as (c) but for FEA recorded von Mises stress.

3. EXPERIMENTS AND RESULTS

The new BMD-adjusted FEA method was successfully applied on three repeat scans of all ten cadaveric specimens used in our experiments. Figure 1 presents qualitative results of FEA over a cylindrical Tb VOI (modulus: 1,157 MPa). Figure 1(a) and (b) illustrate the VOI selection and FEA application processes. The average number of vertex and voxel volume elements on the top surface of a cylindrical VOI were 2,159 and 2,108 respectively. The average number of vertices, edges, and volume elements over a VOI were 102,167; 301,921; and 97,637 respectively. Mean ± standard deviation (std) of the computed Young's modulus from all specimens was 1,165.44 ± 318.46 MPa and the average running time for FEA on a VOI was 3.12 ± 0.52 minutes. Color-coded illustrations of CHA density map and FEA based von Mises stress over the target Tb VOI are shown in (c) and (d), respectively. Visual correspondence between Tb microstructures (red) in (c) and high stress lines (red) in (d) may be noted, which supports the central hypothesis that stress primarily propagates through Tb voxels with high stiffness compared to the marrow voxels with low stiffness.

Results of linear correlation analysis evaluating the relationship between FEA computed von Mises stress and CHA density is presented in Figure 2(a). A high linear correlation ($r = 0.87$) was observed between computed von Mises stress and CHA density at individual voxels, which further validates the qualitative observations of Figure 1 and the principle of our BMD-adjusted FEA. Normalized stress histograms were computed over segmented Tb and marrow regions of all ten specimens[43] and the result is shown in Figure 2(b). As can be seen from the stress histogram over marrow region (green), large number of marrow voxels experience lower stress and the number rapidly falls toward zero with increasing stress values. On the other hand, histogram computed over Tb region (red) shows high percentage of Tb voxels with higher values of stress with the peak at 37.00 ± 15.05 MPa. Furthermore, an unpaired t-test between the stress values computed from Tb and marrow region shows significant difference ($p < 10^{-7}$) in stress distribution over the two regions.

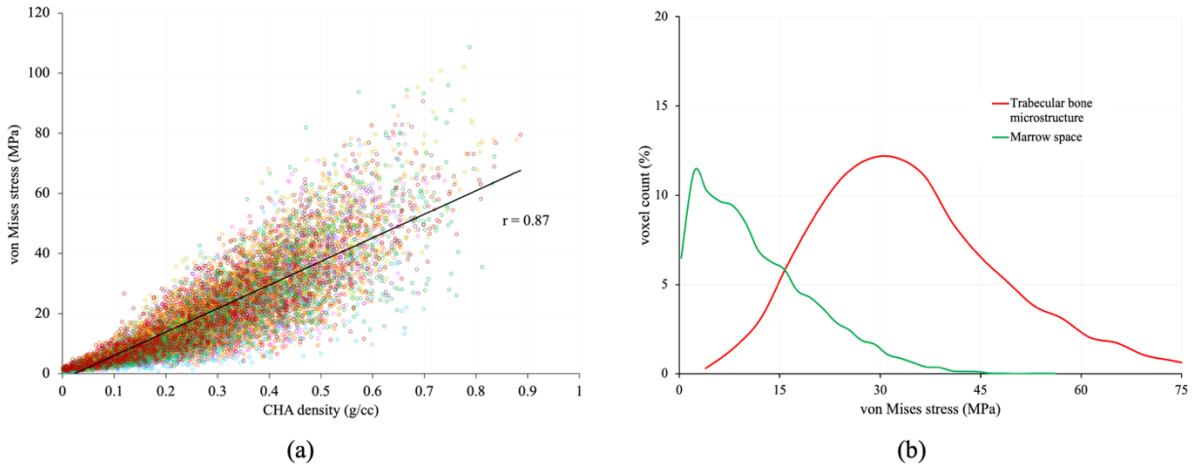

Figure 2. Quantitative evaluation of multi-row detector CT (MDCT)-based FE modelling. (a) Linear correlation (r-value) between computed von Mises stress and CHA density at individual voxels on axial slices at the middle of the specimen along its length. (b) Normalized stress histogram over segmented trabecular bone microstructure and marrow regions.

Results of repeat scan reproducibility analysis is shown in Figure 3. Average Young's modulus values computed from the three sets of repeat scans were 1,176.15 ± 348.88, 1,153.69 ± 317.41, and 1,166.48 ± 322.54 MPa respectively. Also, a high repeat MDCT scan reproducibility (ICC = 0.98) (n=10) of FEA-derived Young's modulus was observed. Both qualitative and quantitative experimental results suggest that the comprehensive protocol of MDCT-based FEA of quantitative Tb microstructural strength as presented in this paper is effective and reproducible.

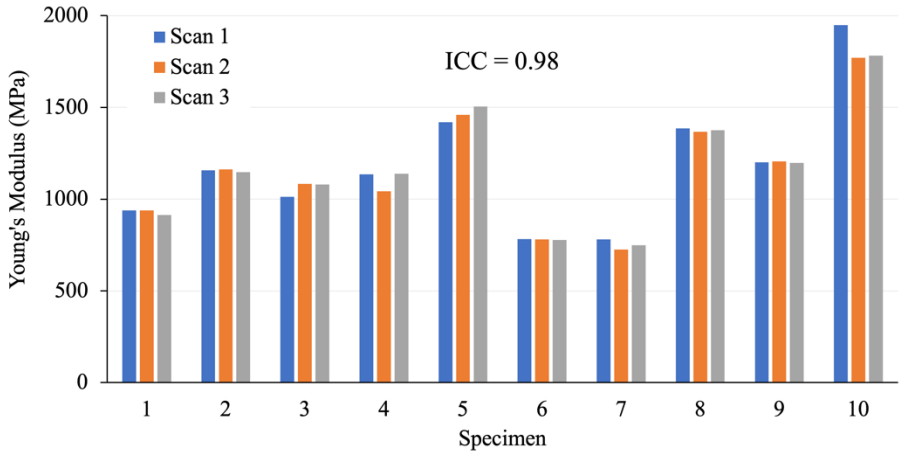

Figure 3. Result of repeat scan reproducibility of MDCT-based FE analysis. Computed Young's modulus from three repeat scans of each specimen are shown.

4. CONCLUSIONS

An emerging MDCT-based method is presented to compute the strength of Tb microstructure using a new BMD-adjusted FE modelling and analytic method. Experimental results have shown that our BMD-adjusted FEA method of computing Tb microstructural strength is reproducible and support the central hypothesis that computational stresses follow Tb microstructure fuzzily characterized by high BMD values at the current regime of *in vivo* CT resolution.

ACKNOWLEDGEMENTS

This work was supported in part by the NIH grant R01 HL142042.

REFERENCES

[1] BL Riggs, S Khosla, and LJ Melton, 3rd, "Better tools for assessing osteoporosis," *Journal of Clinical Investigation*, **122**, 4323-4324, 2012, PubMed Central PMCID: PMC3533568.

[2] T Sözen, L Özışık, and NÇ Başaran, "An overview and management of osteoporosis," *European Journal of Rheumatology*, **4**, 46-56, 2017.

[3] NC Wright, AC Looker, KG Saag, JR Curtis, ES Delzell, S Randall, and B Dawson-Hughes, "The recent prevalence of osteoporosis and low bone mass in the United States based on bone mineral density at the femoral neck or lumbar spine," *Journal of Bone and Mineral Research*, **29**, 2520-2526, 2014.

[4] LJ Melton, 3rd, SH Kan, HW Wahner, and BL Riggs, "Lifetime fracture risk: an approach to hip fracture risk assessment based on bone mineral density and age," *J Clin Epidemiol*, **41**, 985-94, 1988.

[5] A Singer, A Exuzides, L Spangler, C O'Malley, C Colby, K Johnston, I Agodoa, J Baker, and R Kagan, "Burden of illness for osteoporotic fractures compared with other serious diseases among postmenopausal women in the United States," Proc. of *Mayo Clinic Proceedings,* **90**, 53-62, 2015.

[6] GJ Kazakia and S Majumdar, "New imaging technologies in the diagnosis of osteoporosis," *Reviews in Endocrine Metabolic Disorders*, **7**, 67-74, 2006.

[7] JE Adams, "Advances in bone imaging for osteoporosis," *Nature Reviews Endocrinology*, **9**, 28-42, 2013.

[8] E Legrand, M Audran, P Guggenbuhl, R Levasseur, G Chales, MF Basle, and D Chappard, "Trabecular bone microarchitecture is related to the number of risk factors and etiology in osteoporotic men," *Microscopy Research and Technique*, **70**, 952-959, 2007.

[9] AM Parfitt, CHE Mathews, AR Villanueva, M Kleerekoper, B Frame, and DS Rao, "Relationships between surface, volume, and thickness of iliac trabecular bone in aging and in osteoporosis - implications for the microanatomic and cellular mechanisms of bone loss," *Journal of Clinical Investigation*, **72**, 1396-1409, 1983.

[10] E Sornay-Rendu, S Boutroy, F Duboeuf, and RD Chapurlat, "Bone microarchitecture assessed by HR-pQCT as predictor of fracture risk in postmenopausal women: the OFELY study," *Journal of Bone and Mineral Research*, **32**, 1243-1251, 2017.

[11] A Litwic, L Westbury, S Carter, K Ward, C Cooper, and E Dennison, "Self-perceived fracture risk in the global longitudinal study of osteoporosis in women: its correlates and relationship with bone microarchitecture," *Calcified Tissue International*, **106**, 625-636, 2020.

[12] G Chang, CS Rajapakse, C Chen, A Welbeck, K Egol, RR Regatte, PK Saha, and S Honig, "3-T MR Imaging of proximal femur microarchitecture in subjects with and without fragility fracture and nonosteoporotic proximal femur bone mineral density," *Radiology*, **287**, 608-619, 2018.

[13] A Hotca, CS Rajapakse, C Cheng, S Honig, K Egol, RR Regatte, PK Saha, and G Chang, "In vivo measurement reproducibility of femoral neck microarchitectural parameters derived from 3T MR images," *Journal of Magnetic Resonance Imaging*, **42**, 1339-1345, 2015.

[14] CS Rajapakse, JF Magland, MJ Wald, XS Liu, XH Zhang, XE Guo, and FW Wehrli, "Computational biomechanics of the distal tibia from high-resolution MR and micro-CT images," *Bone*, **47**, 556-563, 2010.

[15] N Zhang, JF Magland, CS Rajapakse, YA Bhagat, and FW Wehrli, "Potential of in vivo MRI-based nonlinear finite-element analysis for the assessment of trabecular bone post-yield properties," *Medical Physics*, **40**, 1-10, 2013.

[16] J Keyak, S Sigurdsson, G Karlsdottir, D Oskarsdottir, A Sigmarsdottir, J Kornak, T Harris, G Sigurdsson, B Jonsson, and K Siggeirsdottir, "Effect of finite element model loading condition on fracture risk assessment in men and women: the AGES-Reykjavik study," *Bone*, **57**, 18-29, 2013.

[17] S Majumdar, D Newitt, A Mathur, D Osman, A Gies, E Chiu, J Lotz, J Kinney, and H Genant, "Magnetic resonance imaging of trabecular bone structure in the distal radius: relationship with X-ray tomographic microscopy and biomechanics," *Osteoporos International*, **6**, 376-385, 1996.

[18] TM Link, S Majumdar, P Augat, JC Lin, D Newitt, Y Lu, NE Lane, and HK Genant, "In vivo high resolution MRI of the calcaneus: differences in trabecular structure in osteoporosis patients," *Journal of Bone and Mineral Research*, **13**, 1175-1182, 1998.

[19] FW Wehrli, PK Saha, BR Gomberg, HK Song, PJ Snyder, M Benito, A Wright, and R Weening, "Role of magnetic resonance for assessing structure and function of trabecular bone," *Topics in Magnetic Resonance Imaging* **13**, 335-355, 2002.

[20] G Chang, SK Pakin, ME Schweitzer, PK Saha, and RR Regatte, "Adaptations in trabecular bone microarchitecture in Olympic athletes determined by 7T MRI," *Journal of Magnetic Resonance in Medicine* **27**, 1089-1095, 2008, PubMed Central PMCID: PMCPMC3850284.

[21] S Boutroy, ML Bouxsein, F Munoz, and PD Delmas, "*In vivo* assessment of trabecular bone microarchitecture by high-resolution peripheral quantitative computed tomography," *The Journal of Clinical Endocrinology and Metabolism*, **90**, 6508-6515, 2005.

[22] M Burrows, D Liu, and H McKay, "High-resolution peripheral QCT imaging of bone micro-structure in adolescents," *Osteoporosis International*, **21**, 515-520, 2010.

[23] R Krug, AJ Burghardt, S Majumdar, and TM Link, "High-resolution imaging techniques for the assessment of osteoporosis," *Radiologic Clinics of North America*, **48**, 601-621, 2010, PubMed Central PMCID: PMC2901255.

[24] B Van Rietbergen, S Majumdar, D Newitt, and B MacDonald, "High-resolution MRI and micro-FE for the evaluation of changes in bone mechanical properties during longitudinal clinical trials: application to calcaneal bone in postmenopausal women after one year of idoxifene treatment," *Clinical Biomechanics*, **17**, 81-88, 2002.

[25] CS Rajapakse, MB Leonard, YA Bhagat, W Sun, JF Magland, and FW Wehrli, "Micro–MR imaging–based computational biomechanics demonstrates reduction in cortical and trabecular bone strength after renal transplantation," *Radiology*, **262**, 912-920, 2012.

[26] C Graeff, W Timm, TN Nickelsen, J Farrerons, F Marín, C Barker, and CC Glüer, "Monitoring teriparatide-associated changes in vertebral microstructure by high-resolution CT in vivo: results from the EUROFORS study," *Journal of Bone and Mineral Research*, **22**, 1426-1433, 2007.

[27] FW Wehrli, GA Ladinsky, C Jones, M Benito, J Magland, B Vasilic, AM Popescu, B Zemel, AJ Cucchiara, and AC Wright, "In vivo magnetic resonance detects rapid remodeling changes in the topology of the trabecular bone network after menopause and the protective effect of estradiol," *Journal of Bone and Mineral Research*, **23**, 730-740, 2008.

[28] W Pistoia, Bv Rietbergen, EM Lochmüller, AC Lill, F Eckstein, and P Rüegsegger, "Estimation of distal radius failure load with micro-finite element analysis models based on three-dimensional peripheral quantitative computed tomography images," *Bone*, **30**, 842-848, 2002.

[29] FW Wehrli, CS Rajapakse, JF Magland, and PJ Snyder, "Mechanical implications of estrogen supplementation in early postmenopausal women," *Journal of Bone and Mineral Research*, **25**, 1406-1414, 2010.

[30] J Keyak, I Lee, D Nath, and H Skinner, "Postfailure compressive behavior of tibial trabecular bone in three anatomic directions," *Journal of Biomedical Materials Research*, **31**, 373-378, 1996.

[31] JH Keyak, TS Kaneko, J Tehranzadeh, and HB Skinner, "Predicting proximal femoral strength using structural engineering models," *Clinical Orthopaedics and Related Research*, **437**, 219-228, 2005.

[32] JA MacNeil and SK Boyd, "Bone strength at the distal radius can be estimated from high-resolution peripheral quantitative computed tomography and the finite element method," *Bone*, **42**, 1203-1213, 2008.

[33] S Boutroy, B Van Rietbergen, E Sornay-Rendu, F Munoz, ML Bouxsein, and PD Delmas, "Finite element analysis based on in vivo HR-pQCT images of the distal radius is associated with wrist fracture in postmenopausal women," *Journal of Bone and Mineral Research*, **23**, 392-399, 2008.

[34] H Liebl, EG Garcia, F Holzner, PB Noel, R Burgkart, EJ Rummeny, T Baum, and JS Bauer, "In-vivo assessment of femoral bone strength using Finite Element Analysis (FEA) based on routine MDCT imaging: a preliminary study on patients with vertebral fractures," *PloS one*, **10**, e0116907, 2015.

[35] NM Rayudu, DP Anitha, K Mei, F Zoffl, FK Kopp, N Sollmann, MT Löffler, JS Kirschke, PB Noël, and K Subburaj, "Low-dose and sparse sampling MDCT-based femoral bone strength prediction using finite element analysis," *Archives of Osteoporosis*, **15**, 1-9, 2020.

[36] TM Link, "Osteoporosis imaging: state of the art and advanced imaging," *Radiology*, **263**, 3-17, 2012, PubMed Central PMCID: PMC3309802.

[37] C Li, D Jin, C Chen, EM Letuchy, KF Janz, TL Burns, JC Torner, SM Levy, and PK Saha, "Automated cortical bone segmentation for multirow-detector CT imaging with validation and application to human studies," *Medical Physics*, **42**, 4553-65, 2015, PubMed Central PMCID: PMC4499051.

[38] EH Meijering, WJ Niessen, JP Pluim, and MA Viergever, "Quantitative comparison of sinc-approximating kernels for medical image interpolation," Proc. of *International Conference on Medical Image Computing and Computer-Assisted Intervention*, 210-217, 1999.
[39] F Linde, I Hvid, and F Madsen, "The effect of specimen geometry on the mechanical behaviour of trabecular bone specimens," *Journal of Biomechanics*, **25**, 359-368, 1992.
[40] C Chen, X Zhang, J Guo, D Jin, EM Letuchy, TL Burns, SM Levy, EA Hoffman, and PK Saha, "Quantitative imaging of peripheral trabecular bone microarchitecture using MDCT," *Medical Physics*, **45**, 236-249, 2018.
[41] PK Saha, R Strand, and G Borgefors, "Digital topology and geometry in medical imaging: a survey," *IEEE Transactions on Medical Imaging*, **34**, 1940-1964, 2015.
[42] DL Logan, *A first course in the finite element method*, Cengage Learning, 2011.
[43] C Chen, D Jin, X Zhang, SM Levy, and PK Saha, "Segmentation of Trabecular Bone for In Vivo CT Imaging Using a Novel Approach of Computing Spatial Variation in Bone and Marrow Intensities," Proc. of *Asian Conference on Computer Vision*, 3-15, 2016.